

**Final Technical Report**  
for  
USGS/NEHRP Award Number 08HQGR0047

**Title:** Implications of Rate and State Friction Models  
for Episodic Slow Slip Events

**PI:** Allan Rubin  
Department of Geosciences  
Princeton University, Princeton, N.J. 08544  
Phone: (609) 258-1506  
Fax (609) 258-1274  
e-mail arubin@princeton.edu

**Award Period:** 02/01/2008 – 01/31/2009

## Abstract

The recent discovery of episodic slow slip and tremor in subduction zones has provided the geophysics community with observations of previously unrecognized styles of fault slip. Because slow slip events increase the stressing rate on the locked (seismogenic) portions of major subduction zones worldwide, they are garnering attention as a potentially important tool for assessing seismic hazards in the US and elsewhere. There are many ways of generating slow slip events in models of rate- and state-dependent friction, and at least three have been proposed: (1) “Standard” steady-state velocity-weakening friction on a fault whose length is properly “tuned”; (2) inelastic dilation of fault gouge with increasing slip speed, accompanied by pore pressure reduction and diffusive recovery; and (3) a transition from steady-state velocity weakening to velocity-strengthening behavior at an appropriate slip speed. As discussed by *Rubin* [2008], mechanism (1) requires rather severe tuning of the fault length, at least for the friction law consistent with the most relevant low-temperature lab experiments. Mechanism (3) has some theoretical justification, but not a lot of supporting lab data for silicates yet. Here we explore mechanism (2). Dilatancy is a very attractive mechanism for generating slow slip because, based on limited lab data, it is expected to dominate rate-and-state friction at the low effective normal stresses inferred for slow slip source regions.

We use a simplified “membrane diffusion” approximation for pore fluid flow, where it is assumed that the fault plane is bordered by a low-permeability gouge zone in which the pore pressure varies linearly from its on-fault value to its far-field value. Pore pressure in this formulation is governed by two dimensionless parameters: The ratio of the timescale for fluid diffusion across the low-permeability layer to the timescale for porosity changes on the fault surface (itself tied to the timescale for changes in state), and a parameter that governs the amount of dilation for a given change in state. The first ratio determines the extent to which the fault behaves as drained (no pore pressure change) or undrained (no fluid flow) during changes in porosity, while the second measures the magnitude of the frictional strength change due to pore pressure changes, relative to that due to rate- and state-dependent friction changes, under undrained conditions. We find that for lab values of the governing parameters, and pore pressures of a few MPa or less, dilatancy stabilizes slow slip well into the region of parameter space where slip in the absence of dilatancy would have been dynamic (and in fact out to the largest fault sizes we have been able to simulate). We find also that the recurrence interval of slow slip events, suitably nondimensionalized, increases with fault size following the same trend as in the absence of dilatancy (but extended to much larger fault sizes). An analytical approximation for the maximum slip speed as a function of the fault size and governing parameters matches the numerical simulations fairly well.

In parallel with this, I have been working with Paul Segall at Stanford University on numerical simulations that use true homogeneous diffusion, which is numerically much more demanding than membrane diffusion. Qualitatively the simulations behave similarly. Using a linear stability analysis for the homogeneous diffusion case, we obtained analytical expressions for the critical stiffness and period of oscillation at neutral stability. These can be used to map values of the governing parameters for homogeneous diffusion onto those for membrane diffusion, and vice versa.

# 1. Introduction

Recently observed episodic slow slip events (SSE), sometimes accompanied by deep low-frequency tremors, in shallow subduction zones [e.g., *Hirose et al.*, 1999; *Dragert et al.*, 2001; *Lowry et al.*, 2001] have been proposed to occur along subduction plate interfaces in the vicinity of highly elevated pore fluid pressure. Several lines of evidence, including deep metamorphic dehydration encountered by subducting slabs, and seismologically inferred high  $v_p/v_s$  and high Poisson’s ratios, suggest the presence of near-lithostatic fluid pressure at the source areas of SSEs and non-volcanic tremors.

Numerical simulations in the framework of rate- and state-dependent friction have demonstrated that short-period aseismic deformation transients can emerge spontaneously when fluid pressure is near lithostatic around the friction stability transition [*Liu and Rice*, 2005, 2007; *Shibazaki and Shimamoto*, 2007; *Rubin*, 2008]. Applying temperature-dependent wet granite [*Blanpied et al.*, 1998] and gabbro [*He et al.*, 2007] rate and state friction parameters in a 2-D subduction earthquake model with the “aging” version of evolution law, *Liu and Rice* [2007, 2009] produced episodic SSEs where the velocity-weakening fault length  $W$  under highly elevated pore pressure is too large for steady sliding but insufficient for dynamic instability; the fault response is determined by the ratio between  $W$  and the critical nucleation size  $h^*$ . The detailed definition of  $h^*$  will be described in the next section. Such numerical simulations can produce spontaneous SSEs with aspects, such as recurrence period and cumulative slip, that are similar to field observations. All the above numerical studies have assumed effective normal stress on the fault to be a time-invariant property during the slow slip sequences. However, both field observations and numerical calculations suggested that fluid pressure on the fault has much influence on the occurrence of SSEs and tremors. In particular, the proposed high fluid pressure, is precisely the condition for which *Segall and Rice* [1995] suggested that fault stabilization by induced suction from dilatancy during increased shear rates becomes most important.

Sufficiently compact granular material dilate as they begin to shear. After a certain amount of deformation, a critical state is reached where porosity and pore pressure are constant [*Schofield and Wroth*, 1968]. For fluid-saturated materials, pore expansion will result in a reduction in pore fluid pressure and an increase in effective normal stress. This dilatancy-strengthening process has been suggested to play a role in inhibiting rapid deformations of landslides [e.g., *Iverson et al.*, 2000], glacier basal sediments [*Clarke*, 1987; *Iverson et al.*, 1998] and fault gouges [*Marone et al.*, 1990; *Lockner and Byerlee*, 1994]. *Sleep and Blanpied* [1992] presented quantitative models of earthquake cycles, in which pore pressure increases due to pore compaction during the interseismic period until a Coulomb slip condition is satisfied, followed by a rapid slip event (model earthquake) with pore pressure dropping to the initial level due to dilatancy. *Sleep* [1995] improved the model by including the explicit instability condition for combined slip weakening, frictional dilatancy and shear heating induced thermal pressurization [*Sibson*, 1973; *Lachenbruch*, 1980; *Mase and Smith*, 1987]. *Segall and Rice* [1995] incorporated both processes of dilatancy and pore compaction into the rate and state friction model, to understand the conditions for unstable slip on saturated fault gouge. They assumed that the actively slipping zone is bordered by a less permeable layer within which pore pressure varies linearly from the level on the slipping interface to the ambient level in the surrounding rock mass. This is called the “membrane diffusion” (or “lumped reservoir”) approximation, previously used by *Rudnicki and Chen* [1988] in an analysis of laboratory experiments. Linearized perturbation analysis of a single-degree-of-freedom spring-slider model at steady sliding shows that slip is always stable when the effective normal stress is smaller than a

threshold which is determined by the fault gouge frictional and hydraulic properties [Segall and Rice, 1995]. The higher the pore pressure on the sliding interface, the more important dilatancy is in stabilizing slip. Taylor and Rice [1998] first included dilatancy in a 2-D subduction fault model with rate and state friction to study its effects on earthquake rupture in the radiation damping approximation [Rice, 1993]. They found that quasi-dynamic seismic rupture slows down or even stops near where effective normal stress is lower than that in the seismogenic zone; without dilatancy seismic slip of several meters would occur where the fault breaches the surface.

Building on Taylor and Rice [1998], Liu and Rice [2005b] and Segall and Rubin [2007], in this study we analyze the conditions for spontaneous short-period aseismic transients on a fluid-infiltrated subduction fault including dilatancy and pore compaction, with the “membrane diffusion” approximation. We show, with a Cascadia-like subduction fault model, that episodic aseismic transients can exist for a much broader range of  $W/h^*$  due to dilatancy stabilization. The cumulative slip per episode and the recurrence period of modeled SSEs are comparable to those at the same  $W/h^*$  without dilatancy. They further follow the approximately linear trend of increasing period with  $W/h^*$  beyond the aseismic-seismic boundary that is defined in the absence of dilatancy. In contrast, the maximum slip velocity during SSE episodes can be several orders of magnitude smaller than those at the same  $W/h^*$  without dilatancy. Furthermore, the difference in maximum velocity among calculations with different dilatancy coefficients becomes more significant at large  $W/h^*$ . Due to the effective stabilization at near-lithostatic pore fluid pressure, we expect aseismic slips to appear for even infinitely large  $W/h^*$ , given appropriate frictional and hydraulic parameters.

## 2. Constitutive models

### 2.1 Rate and state friction

We use a single-state-variable form of the rate and state-dependent friction law, in which the frictional resistance  $\tau$  is a function of the sliding velocity  $V$  and the state variable  $\theta$ . In particular,

$$\tau = \bar{\sigma} f = (\sigma - p) \left[ f_0 + a \ln \left( \frac{V}{V_0} \right) + b \ln \left( \frac{V_0 \theta}{d_c} \right) \right], \quad (1)$$

where effective normal stress  $\bar{\sigma}$  is the difference between the normal stress applied on the fault  $\sigma$  and pore pressure  $p$ ;  $a$  and  $b$  are rate and state friction parameters,  $V_0$  is a reference velocity and  $d_c$  is a characteristic slip distance over which state evolves.  $f_0$  is a nominal friction when  $V = V_0$  at steady state. In this study, for computational convenience we use the “aging” state evolution law, which permits friction to evolve even on stationary contacts

$$\frac{d\theta}{dt} = 1 - \frac{V\theta}{d_c}. \quad (2)$$

The steady state friction  $f_{ss} = f_0 + (a - b) \ln(V/V_0)$  is reached when  $\theta = \theta_{ss} = d_c/V$ . The constitutive parameters  $a$  and  $b$  are interpreted as the instantaneous changes in  $f$  and  $f_{ss}$ , respectively, in response to a velocity step:  $a = V(\partial f / \partial V)_{inst}$  and  $a - b = V(df_{ss}/dV)$ . For  $a - b > 0$ , the sliding surface is steady state velocity-strengthening and slip is stable. For  $a - b < 0$ , the interface is steady state velocity-weakening and unstable slip is possible when, for a single-degree-of-freedom spring-slider system subject to small perturbations from steady sliding, the spring stiffness  $k$  is less

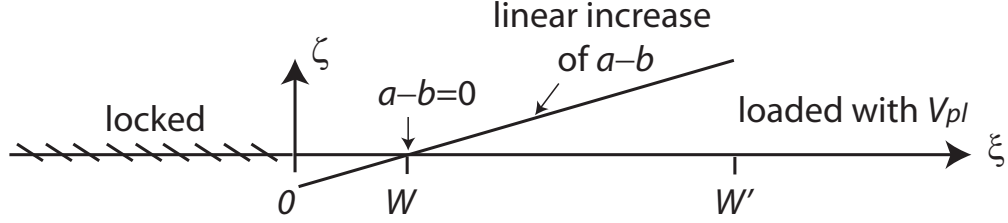


Figure 1: Geometry and  $a - b$  distribution for the 1D spatially periodic fault model. The fault is locked at  $-8W < \xi < 0$ , velocity-weakening at  $0 \leq \xi \leq W$ , velocity-strengthening at  $W < \xi \leq W'$ , and loaded by a constant  $V_{pl}$  at  $W' < \xi < W' + 8W$ .  $W'/W = 4$  for most simulation cases if not otherwise stated.  $a - b$  linearly increases from -0.004 to 0.012, and  $b = 0.034$  is uniform between  $0 \leq \xi \leq W'$ .

than the critical stiffness  $k_{cr} = \bar{\sigma}(b - a)/d_c$ . A critical cell size  $h^*$  is defined by equating  $k_{cr}$  to the effective stiffness  $k = \gamma\mu'/h$  at the center of a crack of length  $h$ . Thus

$$h^* = \gamma \frac{\mu' d_c}{\bar{\sigma}(b - a)}. \quad (3)$$

Here,  $\gamma$  is a model-dependent constant of order unity;  $\gamma = 2/\pi$  when using the cellular basis set for slip on a crack that is not too close to the surface in *Rice* [1993].  $\mu'$  is the effective shear modulus ( $\mu' = \mu$  for anti-plane strain and  $\mu/(1 - \nu)$  for plane strain deformation, where  $\nu$  is Poisson's ratio); we  $\mu = 30$  GPa and  $\nu = 0.25$ . In the definition of  $h^*$ , we use the average value  $\langle b - a \rangle$  over a fault length where  $b - a$  depth distribution is not uniform.

## 2.2 Governing equations for the fluid

We follow *Segall and Rice* [1995] and *Taylor and Rice* [1998] in the treatment of pore fluid diffusion and pore compaction associated with friction evolution. For the 2-D model considered here, we assume that fluid (water) flux is limited to the direction  $\zeta$  perpendicular to the fault and that there is no flux in the direction  $\xi$  parallel to the fault (Figure 1). The conservation of fluid mass implies that

$$\frac{\partial q_m}{\partial \zeta} + \frac{\partial m}{\partial t} = 0, \quad (4)$$

where  $m$  is the fluid mass per unit volume of rock, and  $q_m$  is the fluid mass flux per unit area. Fluid flux is related to the pore pressure gradient via Darcy's law:

$$q_m = -\frac{\rho\kappa}{\eta} \frac{\partial p}{\partial \zeta}, \quad (5)$$

where  $\rho$  is the fluid density,  $\kappa$  is the permeability for diffusion normal to the fault and  $\eta$  is the fluid viscosity. The rate of fluid mass change can be written as

$$\frac{\partial m}{\partial t} = \phi \frac{\partial \rho}{\partial t} + \rho \frac{\partial \phi}{\partial t} = \rho\beta \left( \frac{\partial p}{\partial t} + \Lambda \frac{\partial \mathcal{T}}{\partial t} + \frac{1}{\beta} \frac{\partial \phi_{pl}}{\partial t} \right) \quad (6)$$

where porosity  $\phi$  is the volume ratio between the pore space and the reference composite and  $\mathcal{T}$  is temperature.  $\beta_f \equiv (1/\rho)(\partial\rho/\partial p)_\mathcal{T}$  is the isothermal fluid compressibility,  $\gamma_f \equiv -(1/\rho)(\partial\rho/\partial \mathcal{T})_p$  is the fluid expansion coefficient at constant pressure,  $\beta_\phi \equiv (1/\phi)(\partial\phi/\partial p)_\mathcal{T}$  is the elastic pore compressibility and  $\gamma_\phi \equiv (1/\phi)(\partial\phi/\partial \mathcal{T})_p$  is pore expansion coefficient. Parameters  $\beta$  and  $\Lambda$  are

defined as  $\beta = \phi(\beta_f + \beta_\phi)$ ,  $\Lambda = (\gamma_\phi - \gamma_f)/(\beta_f + \beta_\phi)$ . Here, the change in porosity is written as the sum of a plastic component  $\phi_{pl}$  and an elastic component, which is related to the changes in  $p$  and  $\mathcal{T}$  via  $\beta_\phi$  and  $\gamma_\phi$  respectively.

Substituting (5) and (6) into (4), we get the pore pressure diffusion equation with a source term from the plastic porosity change and temperature change

$$c \frac{\partial^2 p}{\partial \zeta^2} - \left( \frac{\partial p}{\partial t} + \Lambda \frac{\partial \mathcal{T}}{\partial t} \right) = \frac{1}{\beta} \frac{\partial \phi_{pl}}{\partial t}, \quad (7)$$

where  $c = \kappa/(\eta\beta)$ . In the following analysis, we neglect the  $\partial \mathcal{T}/\partial t$  term as the temperature variation during slow slip events is considered to be small. For the flux normal to the fault, we make the “membrane diffusion” approximation so that equation (7) can be written as

$$\frac{\partial p}{\partial t} = -\frac{p - p_0}{t_p} - \frac{1}{\beta} \frac{\partial \phi_{pl}}{\partial t}. \quad (8)$$

Here  $t_p = \eta\beta d_p^2/\kappa$  is a characteristic time for  $p$  to re-equilibrate with its ambient value  $p_0$ . As discussed in *Segall and Rice* [1995], this approximation is appropriate when the slipping zone is bordered by a layer of thickness  $d_p$  less permeable than either the slipping interface or the surrounding rock mass, and times are long compared to the diffusion time across that layer.

We model the dilatancy term following the analysis in *Sleep* [1995] and *Segall and Rice* [1995], which build on observations from fault gouge friction experiments at room temperature [*Marone et al.*, 1990]. The plastic component of porosity is assumed to evolve with the state variable  $\theta$  as

$$\phi_{pl} = \phi_0 - \epsilon \ln \left( \frac{V_0 \theta}{d_c} \right), \quad (9)$$

where  $\phi_0$  is a reference porosity and  $\epsilon$  is the dilatancy coefficient. Equation (8) then becomes

$$\frac{\partial p}{\partial t} = -\frac{p - p_0}{t_p} + \frac{\epsilon}{\beta} \frac{1}{\theta} \frac{d\theta}{dt}. \quad (10)$$

The rate and state friction law (equations (1) and (2)) and pore pressure evolution (equation (10)) are implemented together with the quasi-dynamic elastic relation between shear stress and slip distributions on the fault, to solve for the history of slip velocity, shear stress and pore pressure on the modeled fault in earthquake cycles including slow slip events. A radiation damping term that is dynamically correct in instantaneous response and in producing quasi-static long-term response is introduced following *Rice* [1993] and *Lapusta et al.* [2000].

### 2.3 Nondimensional parameters

As is evident from equation (10), two competing factors control the rate of pore pressure change. The first is the rate at which  $p$  communicates with  $p_0$  at the characteristic diffusion time scale  $t_p$ . The second is the rate at which  $p$  changes due to the opening or closing of pore spaces as the state variable  $\theta$  evolves at the time scale  $d_c/V_{ss}$ .  $V_{ss}$  is sliding velocity at steady state. The drainage of the sliding interface is thus characterized by a nondimensional parameter

$$T = t_p/(d_c/V_{ss}). \quad (11)$$



When  $T \ll 1$ , the fault gouge is nearly drained, and there is no change in pore pressure. When  $T \gg 1$ , the system is approaching an undrained condition, and there is no change in fluid mass. On a completely drained fault  $p$  instantaneously re-equilibrates with  $p_0$ ; solutions to the coupled equations are essentially the same as those to the system without dilatancy.

By comparing the *Marone et al.* [1990] laboratory data to their simulations based on the above analysis, *Segall and Rice* [1995] estimated the dilatancy coefficient  $\epsilon$  to be  $1.7 \times 10^{-4}$  for quartz sand under drained conditions. Recently, velocity-stepping friction experiments were conducted on various gouge layer compositions, including angular quartz sand, kaolinite gouge, Westerly granite gouge and clay-rich materials from ODP leg 1175 [*Samuelson et al.*, 2008]. Early results from the clay-rich ODP gouge indicate a trend of  $\epsilon$  decreasing with the normal stress. Estimated dilatancy coefficient is within the range of  $10^{-5}$  to  $10^{-4}$ , consistent with  $\epsilon$  inferred from previous experiments [*Marone et al.*, 1990; *Lockner and Byerlee*, 1994]. Bulk compressibility  $\beta [= \phi(\beta_f + \beta_\phi)]$  can be estimated following the choices in *Segall and Rice* [1995]. Take water compressibility  $\beta_f \sim 5 \times 10^{-4} \text{ MPa}^{-1}$ , elastic pore compressibility  $\beta_\phi \sim 10^{-2} \text{ MPa}^{-1}$  for crystalline rocks that are more representative of fault gouge at seismogenic depths, and a low porosity  $\phi = 0.05$  due to greater densification at depths caused by solution transport and mineralization processes, the bulk compressibility is  $\beta \sim 5 \times 10^{-4} \text{ MPa}^{-1}$ . We note that  $\epsilon$  and  $\beta$  enter equation (10) only through the ratio  $\epsilon/\beta$ , which has the unit of pressure. Therefore, in the following calculations, instead of specifying individual values of  $\epsilon$  and  $\beta$ , we only specify  $\epsilon/\beta$ , in the vicinity of 0.34 MPa based on the above estimates.

Including the pore pressure change with slip, we can write the peak-to-residual stress as  $\Delta\tau^{p-r} = \bar{\sigma}_0\Delta f^{p-r} - f_0\Delta p^{p-r}$  and the total stress drop (difference between initial and residual stresses) as  $\Delta\tau^{i-r} = \bar{\sigma}_0\Delta f^{i-r} - f_0\Delta p^{i-r}$ . For a hypothetical velocity jump from  $V_1$  to  $V_2$  associated with an expanding nucleation zone, the maximum pore suction during the state evolution process on a completely undrained fault is

$$\Delta p^{p-r} = (\epsilon/\beta) \ln(V_2/V_1), \quad (12)$$

when slip is significantly larger than  $d_c$ . Following the approximations of  $\Delta f^{p-r} \approx b\bar{\sigma}_0 \ln(V_2/V_1)$  and  $\Delta f^{i-r} \approx (b-a)\bar{\sigma}_0 \ln(V_2/V_1)$  appropriate for large velocity jumps [*Rubin and Ampuero*, 2005; *Ampuero and Rubin*, 2008], the above two stress drops can be written as

$$\Delta\tau^{p-r} \approx b\bar{\sigma}_0(1-E) \ln(V_2/V_1), \quad (13)$$

and

$$\Delta\tau^{i-r} \approx b\bar{\sigma}_0(1-a/b-E) \ln(V_2/V_1), \quad (14)$$

where the nondimensional parameter

$$E = f_0(\epsilon/\beta)/(b\bar{\sigma}_0) \quad (15)$$

measures the relative contributions from pore suction and friction evolution.

Before performing numerical calculations, some aspects of the nucleation process with dilatancy can be predicted based on the above equations. When  $E \ll 1 - a/b$ , pore pressure changes are irrelevant because the stress drops are dominated by the friction evolution term. When  $1 - a/b < E < 1$ , dilatancy might inhibit nucleation by decreasing the mechanical energy release rate even though the fracture energy is still dominated by the stress drop due to friction. In the case

of a completely undrained fault as shown in equations (13) and (14), the total stress drop becomes negative which predicts no instability. When  $E \geq 1$ , if  $T$  is sufficiently large that the fault is effectively undrained at seismic slip rates, then pore pressure changes will be certain to impede the nucleation, which may develop into slow slip events rather than earthquakes.

The above arguments show that dilatancy has several appealing attributes for promoting the occurrence of slow slip events. First, with certain degree of drainage (roughly speaking,  $t_p/(d_c/V) \geq 1$ ) the nondimensional parameter  $E$  controls whether the nucleation can develop into a dynamic rupture or a slow slip event. Near-lithostatic pore pressure in the slow slip source region implies large  $E$ , and would help to promote slow slips. For example, if we take some representative values  $f_0 = 0.6$ ,  $\epsilon = 1.7 \times 10^{-4}$ ,  $\beta = 5 \times 10^{-4} \text{ MPa}^{-1}$ ,  $b = 0.006$  as inferred by *Segall and Rice* [1995],  $\bar{\sigma}_0 < 33 \text{ MPa}$  will result in  $E > 1$ . Second, when  $E > 1$  is satisfied, slip velocity during the slow slip events can vary several orders of magnitude between, approximately,  $V_{pl}$  and  $V_{dyn}$  (dynamic slip rate), as the drainage  $T = t_p/(d_c/V)$  varies with  $V$ .

### 3. Simplified spectral model

To investigate the effects of dilatancy on aseismic deformation transients, we first study the contributions of various parameters in a simplified model fault that is locked for  $\xi < 0$  and loaded with a constant rate  $V_{pl}$  for  $\xi > W'$ , as shown in Figure 1. Rate and state friction is applied on  $0 \leq \xi \leq W'$ , where slip is velocity-weakening ( $a - b < 0$ ) on  $0 \leq \xi \leq W$  and velocity-strengthening ( $a - b > 0$ ) on  $W < \xi \leq W'$ . Specifically,  $a - b$  linearly increases from  $-0.004$  to  $0.012$ ,  $b = 0.034$  and  $d_c = 0.04 \text{ mm}$  are uniform between  $0 \leq \xi \leq W'$ . Results based on a more realistic Cascadia-like 2-D subduction fault with depth-variable friction parameters and free surface effect will be presented in the next section.

Several length ratios shown in Figure 1 are of different extent of relevance to the simulation results. First, the fault lengths of the “locked” and “loaded” parts have very minor effects, as verified numerically, when they are much larger than  $W$ . We use  $8W$  for both segments in the spatially periodic model. Second, as pointed out by *Rubin* [2008], the ratio  $W'/W$  continues to influence the results even when it gets sufficiently large, because the enforced  $V = V_{pl}$  at  $\xi > W'$  introduces a discontinuity in velocity gradient  $dV/d\xi$  at  $\xi = W'$ , which has no counterpart in nature. Among the numerically calculated physical properties,  $W'/W$  has relatively small effects on the sliding pattern (i.e., stable, periodic, or unstable) and the maximum velocity during aseismic slip events.  $W'/W$  has a more significant influence on the recurrence interval of aseismic events, but to the first order that can be accounted for by its influence on the steady slip speed  $V_{ss}$  at a representative point within  $W$  (e.g.,  $W/2$ ). *Rubin* [2008, eqn. 22] showed that for infinitely locked and loaded regions and  $W'/W \gg 1$ , the steady slip speed at the center of  $W$  is

$$V_{ss} \approx \frac{\sqrt{2}}{\pi} \left( \frac{W}{W'} \right)^{1/2} V_{pl}, \quad (16)$$

and recurrence period varies inversely with this  $V_{ss}$ . For  $W'/W = 4$  used in this study,  $V_{ss} \approx 0.23V_{pl}$  at  $\xi = W/2$  is used in the definition of  $T$  (equation 11).

Finally, we learned from 2-D subduction fault simulations [*Liu and Rice*, 2007] that the ratio between the length of the fault that slides at velocity-weakening under extremely high fluid



pressure at the critical nucleation size, namely

$$\frac{W}{h^*} = \frac{\pi W \langle b - a \rangle \bar{\sigma}_0}{2\mu' d_c}, \quad (17)$$

also affects the fault response. As  $W/h^*$  increases, fault slip proceeds from steady state, to simple periodic, to complex periodic or aperiodic, to seismic. We show that, in addition to parameters  $E$  and  $T$  that are directly related to the pore pressure evolution,  $W/h^*$  continues to be an important factor in determining the fault response.

### 3.1 The effect of $W/h^*$

For the simplified spectral model, the average  $b - a$  over  $W$  is  $\langle b - a \rangle = 0.002$ . We keep  $W = 20$  km and  $d_c = 0.04$  mm in all simulations and vary  $\bar{\sigma}_0$  to achieve a wide range of  $W/h^*$ . For example,  $\bar{\sigma}_0 = 0.6$  MPa results in  $W/h^* \approx 23.5$ .

For selected combinations of dilatancy parameters  $E$  and  $T$ , Figure 2 summarizes (a) the maximum slip rate, normalized by  $V_{pl}$ , during episodes of modeled SSEs, and (b) the recurrence period, defined as the interval between two adjacent  $V_{max}$  peaks in time domain, as functions of  $W/h^*$ , compared to calculations without the dilatancy effect. When pore pressure is assumed to be time-invariant (black solid dots), similar to the results in *Liu and Rice* [2007] and *Rubin* [2008], simple periodic oscillations with  $V_{max} \geq V_{pl}$  start to appear at  $W/h^* \gtrsim 3$ , followed by “period doubling” oscillations (two dots at one  $W/h^*$ ) for  $W/h^* \approx 16$ . The difference between  $V_{max}$  of two events in one “period doubling” episode increases with  $W/h^*$ . The vertical dashed line at  $W/h^* \approx 24$  represents the “abrupt” jump from aseismic to seismic slip rates, and is approximately  $(12/\pi^2)[b/\langle b-a \rangle]h^*$ , similar to that estimated by *Rubin* [2008] with  $W'/W = 5$  and linear gradient in  $a/b$ .

Open symbols represent calculations including the dilatancy effect. We choose three sets of parameters:  $E = 1, T = 0.23$ ;  $E = 1, T = 0.046$ ; and  $E = 0.1, T = 0.23$ , to investigate how different combinations of dilatancy and diffusion parameters affect the process. A general observation from all the dilatancy calculations in Figure 2(a) and (b) is that aseismic oscillations now exist over a much broader range of  $W/h^*$ . For all the three sets of parameters,  $V_{max}$  remains less than  $10^3 V_{pl}$  up to  $W/h^* \approx 70$ , the largest in our calculations to maintain a resolution of  $L_b/\Delta\xi = (\mu' d_c/b\bar{\sigma}_0)/\Delta\xi > 3$  (most cases have the ratio between 5 and 9);  $\Delta\xi$  is grid spacing. We expect that  $V_{max}$  remains aseismic for sufficiently larger values of  $W/h^*$ , when  $E$  and  $T$  are both of order 1. At  $W/h^* \lesssim 23$ , slow slip events produced with the inclusion of dilatancy appear as simple periodic or periodic doubling episodes, with small variations in  $V_{max}$  and  $T_{cyc}$ .  $V_{max}$  is generally slower than those with constant  $\bar{\sigma}$ ;  $V_{max}$  at  $W/h^* = 23.5$ ,  $E = 1$  and  $T = 0.23$  is nearly one order of magnitude smaller. At  $W/h^* > 23$ ,  $V_{max}$  and  $T_{cyc}$  continue to increase, with much greater variation ranges at each  $W/h^*$ .

### 3.2 The effects of $E$ and $T$

Figure 3 shows the variation of maximum aseismic slip velocity and recurrence period with  $T$  ( $E = 1$  fixed) and  $E$  ( $T = 0.23$  fixed), respectively, at  $W/h^* = 23.5$ .

For  $T \ll 1$ , fluid pressure quickly re-equilibrates with the ambient level and thus the fault response approaches that of the no-dilatancy situation. In Figure 3(a), the smallest  $T = 0.0023$  case produces period doubling aseismic sequences, with the high and low velocities at  $18V_{pl}$  (=

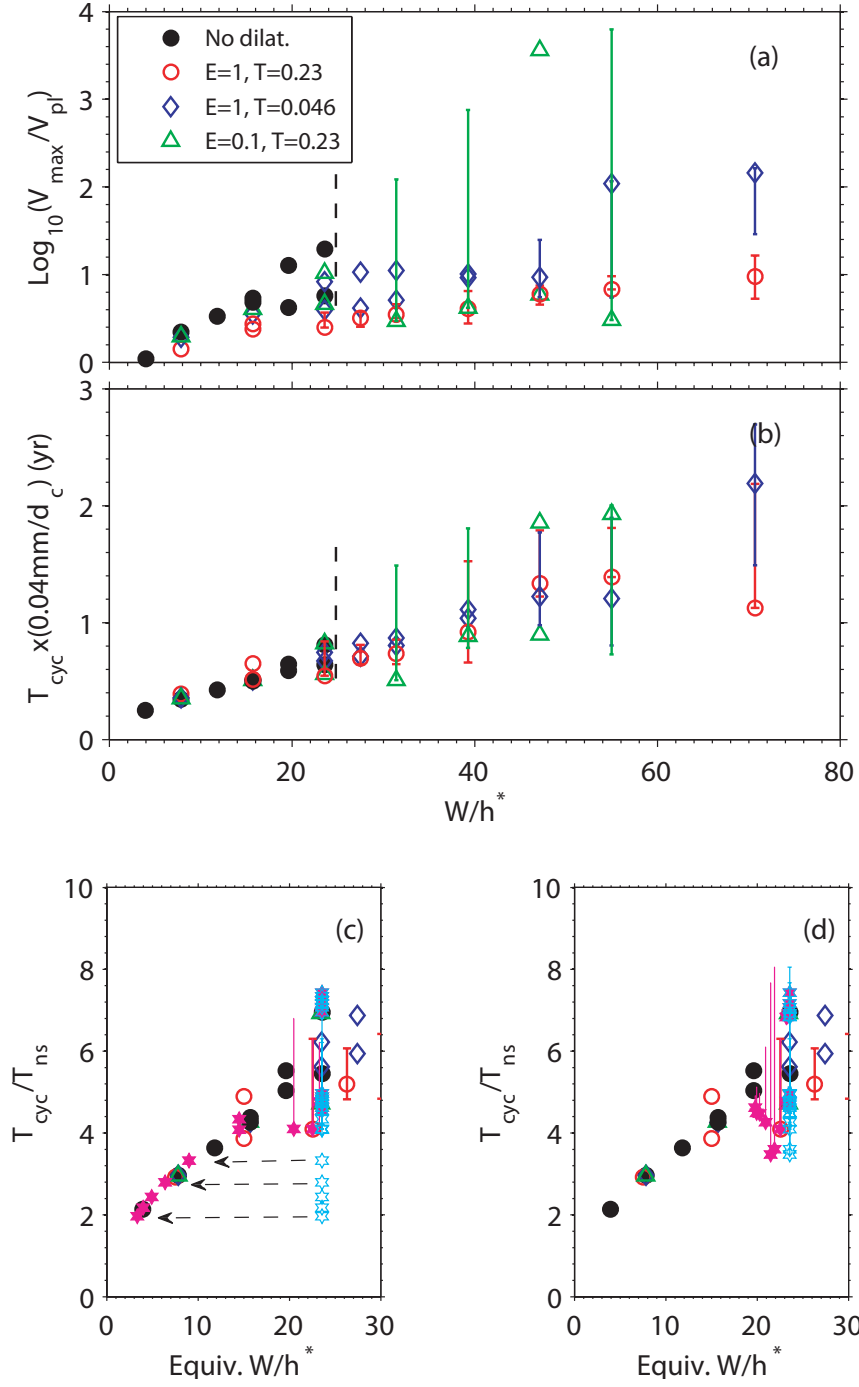


Figure 2: (a) Maximum slip velocity  $V_{\max}$  (normalized by  $V_{pl}$ ) and (b) recurrent period  $T_{cyc}$  as a function of  $W/h^*$  for simulation cases with (open symbols) and without (black solid dots) dilatancy. Several combinations of nondimensional parameters  $E$  and  $T$  are chosen in the dilatancy cases: red circles  $E = 1, T = 0.23$ ; blue diamonds  $E = 1, T = 0.046$ ; green triangle  $E = 0.1, T = 0.23$ . (c)  $T_{cyc}$  normalized by neutral stability period  $T_{ns}(E, T, a/b)$ , for fixed  $E = 1$  and  $a/b = 0.94$ . Open cyan hexagams represent cases in Figure 3(c). Solid magenta hexagams are the same cases but with adjusted  $W/h^*$  according to equation (18). (d) Same as in (c), but the variation in  $E$ ;  $T = 0.23$  and  $a/b = 0.94$  are fixed.  $W/h^*$  for the dilatancy cases in (b) are also adjusted to plot in (c) and (d).

$2.12 \times 10^{-8}$  m/s) and  $5.2V_{pl}$  and recurrence periods of 0.80 and 0.63 yr, respectively. These are very close to the velocities of  $19V_{pl}$  and  $5.7V_{pl}$  and recurrence periods of 0.81 and 0.64 yr, for the same  $W/h^* = 23.5$  but without dilatancy. As  $T$  increases toward 1, the average  $V_{max}$  decreases while the recurrence period remains relatively constant. This behavior can be explained by the amplitude and duration of pore suction and the following recovery stage. Figure 4(a) shows the change in effective normal stress  $\Delta\bar{\sigma} = -(p - p_0)$ , normalized by the initial  $\bar{\sigma}_0$ , at  $\xi = W/4$ , for sequences of aseismic events modeled at  $T \leq 1$ . At  $T$  increases from 0.0023 to 0.23, the deviation of  $\bar{\sigma}$  from its ambient level becomes higher and takes longer durations. Smaller  $V_{max}$  is resulted when the fault slips at a higher  $\bar{\sigma}$ . However, due to the compensating effects of smaller velocity and longer sliding duration, the recurrence period remains relatively constant for  $T \lesssim 1$ .

For  $T \gg 1$ , the fault zone is considered nearly undrained so that pore suction remains for a much longer duration than the state evolution time, and sliding velocity approaches steady state. In Figure 3(a),  $V_{max}$  (for the velocity-weakening zone) approaches its steady state value of  $V_{ss} \approx V_{pl}/3$  at  $\xi = W$ . Figure 4(b) shows  $\Delta\bar{\sigma}/\bar{\sigma}_0$  for several cases with  $T > 1$ . The amplitude of  $\Delta\bar{\sigma}$  does not change much as  $T$  increases from 1.15 to 3.45, but the duration when  $\bar{\sigma}$  is off its ambient level becomes longer for larger  $T$ . Thus, although the variation in velocity is nearly negligible at  $T > 1$ , sliding at velocities higher than  $V_{ss}$  for longer durations will result in larger cumulative slip that implies a longer recurrence period. This explains the increase in  $T_{cyc}$  for  $T > 1$ .

Considering the dilatancy effect, *Segall et al.* [2010] derived the critical stiffness  $k_{cr}$  and neutral stability period  $T_{ns}$  as functions of parameters  $E$  and  $T$ , using linearized stability analysis for a single-degree-of-freedom spring-slider system. Their analytical solutions predict that for  $E = 1$  and  $a/b = 0.94$  as in the simulations of the left column in Figure 3, the normalized critical stiffness  $k_{cr}^{dilat}/k_{cr}^{drain}$  quickly drops from 1 to nearly 0 as  $T$  increases from 0.1 to 100;  $k_{cr}^{dilat}/k_{cr}^{drain} = 0.05$  at  $T = 20$ . Thus, for the particular parameters  $E$  and  $a/b$ , the equivalent  $W/h^* = Wk_{cr}/(\gamma\mu')$  decreases as  $T$  becomes larger than 0.1, resulting in a decreasing ratio of  $T_{cyc}/T_{ns}$  for  $T > 0.1$  as shown in Figure 3(c). As a correction, for each simulation shown in the left column of Figure 3, we calculated the equivalent  $\langle W/h^* \rangle^{dilat}$  using the proportionality

$$\frac{\langle W/h^* \rangle^{dilat}}{\langle W/h^* \rangle^{drain}} = \frac{k_{cr}^{dilat}}{k_{cr}^{drain}}(E, T, a/b). \quad (18)$$

As shown in Figure 2(c), each open cyan hexagram originally aligned at  $W/h^* = 23.5$  is adjusted to a smaller equivalent  $W/h^*$  and is represented by a solid magenta hexagram. The largest adjustment from  $\langle W/h^* \rangle^{drain} = 23.5$  to  $\langle W/h^* \rangle^{dilat} \approx 3.3$  occurs for the largest  $T \approx 7$ . We can see from Figure 2(c) that the adjusted  $T_{cyc}/T_{ns}$  versus  $W/h^*$  for choices of  $T$  over three orders of magnitude agrees very well with the trend defined by the no-dilatancy and limited selections of  $(E, T)$  simulations. Adjustments to the dilatancy cases as shown in Figure 2(b) and (c) are negligible due to the small  $T \leq 0.23$ .

The effects of parameter  $E$  ( $T = 0.23$  fixed) are similar to that of parameter  $T$ . For  $E \ll 1$ , both  $V_{max}$  and  $T_{cyc}$  approach the values without dilatancy because the pore suction is negligible compared to the initial  $\bar{\sigma}_0$ . The average  $V_{max}$  decreases as  $E$  increases toward 1, as higher pore suction is induced by larger porosity changes (Figure 4(c)). Recurrence period remains relatively constant for  $E < 1$  due to the compensating effects of smaller velocity and longer sliding duration.  $T_{cyc}$  increases with  $E > 1$ , as the increase in event duration becomes much more dominant than the small variations in sliding velocity. The increase of  $T_{cyc}$  with  $E$  can be approximately adjusted by the neutral stability period  $T_{ns}$ , as opposed to the decreasing trend in Figure 3(c), because for the

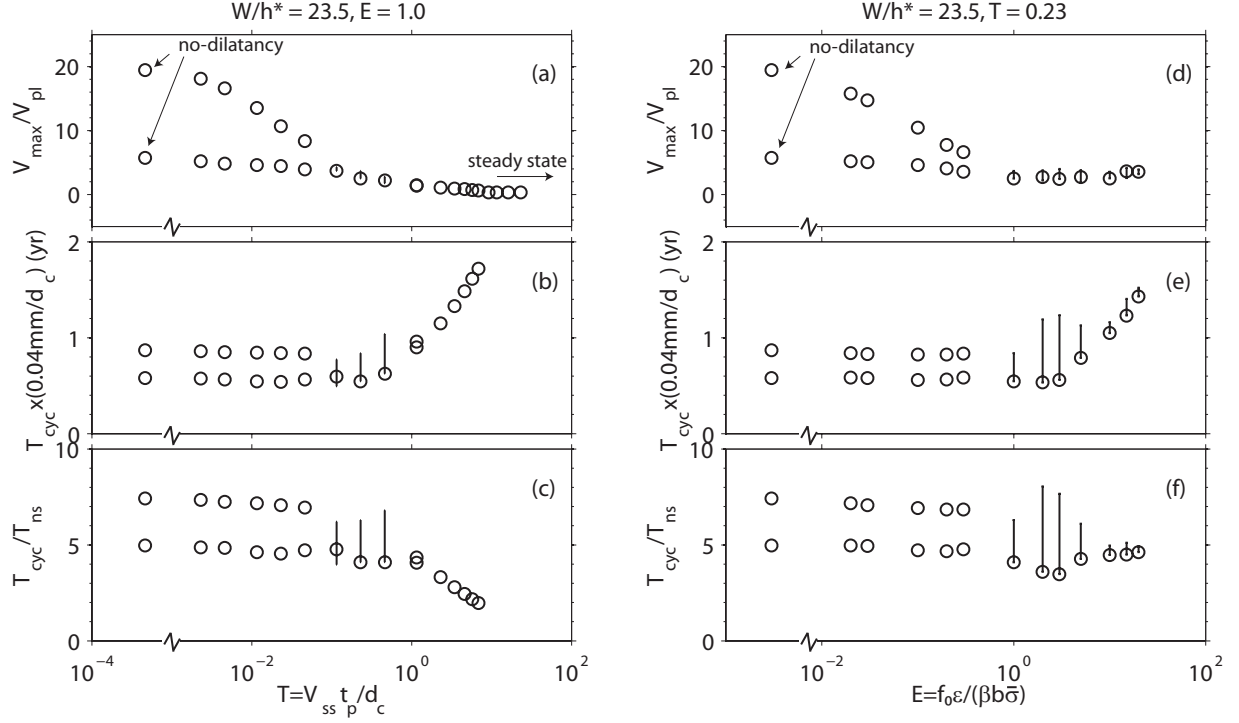


Figure 3: Left column (a)-(c): maximum slip velocity  $V_{max}$  (normalized by  $V_{pl}$ ), recurrent period  $T_{cyc}$  and  $T_{cyc}$  normalized by the neutral-stability period  $T_{ns}$  variations with nondimensional  $T = V_{ss} t_p / d_c$  ( $E = 1$  fixed). Right column (d)-(f):  $V_{max}$ ,  $T_{cyc}$  and  $T_{cyc} / T_{ns}$  variations with nondimensional  $E = f_0(\epsilon / \beta) / (b \bar{\sigma})$  ( $T = 0.23$  fixed), at  $W/h^* = 23.5$ . The scaling of  $T_{cyc}$  with  $d_c$  makes it possible to label the recurrence period axis with the factor  $0.04 \text{ mm} / d_c$  so that the solutions can be interpreted for other choices of  $d_c$ .

fixed  $T = 0.23$  and  $a/b = 0.94$  the variation of critical stiffness with  $E$  is very small. For example,  $k_{cr}^{dilat}/k_{cr}^{drain} \approx 0.83$  at  $E = 50$ . As a result, the adjustments in  $W/h^*$  are relatively small as shown in Figure 2(d). The adjusted  $T_{cyc}/T_{ns}$  versus  $W/h^*$  still agrees well with the trend defined by the no-dilatancy and limited choices of  $(E, T)$  cases.

## 4. 2-D subduction fault model

In this section, we investigate the effect of dilatancy and pore compaction on a 2D fluid-infiltrated subduction fault. The fault model is set up similarly to that in *Liu and Rice* [2007, 2009], and is summarized here in Figure 5. We simulate the thrust fault by a planar frictional interface in an elastic half-space, with a 2-D plane strain assumption. As a simple representation of the northern Cascadia shallow subduction geometry, the fault dips at a constant angle of  $12^\circ$ .  $\xi$  now starts from the trench and aligns with the down-dip direction. Rate and state-dependent friction is applied on the interface from  $\xi = 0$  to  $\xi = W' = 300$  km. Further down-dip the fault is loaded by a constant plate convergence rate  $V_{pl} = 37$  mm/yr. Friction parameters  $a$ ,  $a - b$  and  $d_c$  are functions of the down-dip distance  $\xi$ , and are invariant with time. For simplicity, we consider the elastic effect of slip on changing only the shear stress; variation in effective normal stress  $\bar{\sigma}$  being the result only of fluctuation in pore pressure  $p$ .

Friction experimental data for gabbro under hydrothermal conditions have recently been reported by *He et al.* [2007]. A tentative application of the gabbro data, as the first set available for a reasonable representation of the seafloor, to a Cascadia-like subduction fault model can produce slow slip events with surface deformation similar to those observed by GPS stations, while models using the wet granite data [*Blanpied et al.*, 1998], which, for lack of a suitable alternative, has been the basis for most previous calculations, result in a very poor fit [*Liu and Rice*, 2009]. Thus, in this paper, we apply the *He et al.* [2007] gabbro friction data in the 2-D fault model. Using a Cascadia subduction zone thermal profile [*Peacock et al.*, 2002], the temperature-dependent  $a - b$  is converted to be depth-dependent as shown in the top panel of Figure 5(b). See *Liu and Rice* [2009] for detailed discussions of the choice of  $a - b$  and application in the 2-D subduction fault model. In the velocity-weakening regime,  $a - b$  remains as a constant of  $-0.0035$  to  $\sim 95$  km, followed by a gradual transition to velocity-strengthening at  $\sim 180$  km.  $a - b$  is about  $0.005$  at the down-dip end of the modeled fault  $W' = 300$  km. Direct effect  $a$  is assumed to increase linearly with the absolute temperature:  $a = 5.0 \times 10^{-5}(\mathcal{T} + 273.15)$ , following an Arrhenius activated process at asperity contacts on the sliding surface [*Rice et al.*, 2001].  $a$  is also converted to be depth-dependent using the *Peacock et al.* [2002] thermal profile.

The down-dip distribution of initial effective normal stress  $\bar{\sigma}_0$  is determined following the discussion of along-dip elevated fluid pressure in *Liu and Rice* [2009], and an example is shown in the middle panel of Figure 5(b). Near the surface and in most part of the seismogenic zone, pore pressure  $p$  is assumed to be the maximum between the hydrostatic pressure  $10[\text{MPa/km}] \times z$  and  $28[\text{MPa/km}] \times z - \bar{\sigma}_{eff}$ ;  $\bar{\sigma}_{eff}$  is a constant level of effective normal stress at depth, taken as 50 MPa in this paper. The low effective normal stress zone extends some distance up-dip ( $W$ ) and down-dip from the friction stability transition, approximately consistent with the seismically inferred depth range of near-lithostatic fluid pressure in northern Cascadia [*Audet et al.*, 2009].  $\bar{\sigma}$  resumes to  $\bar{\sigma}_{eff} = 50$  MPa down-dip to  $W' = 300$  km.

Similar to that in the simplified spectral model,  $W/h^*$  as defined in equation (17) is an important parameter that determines whether the system can produce self-sustained aseismic oscillations.

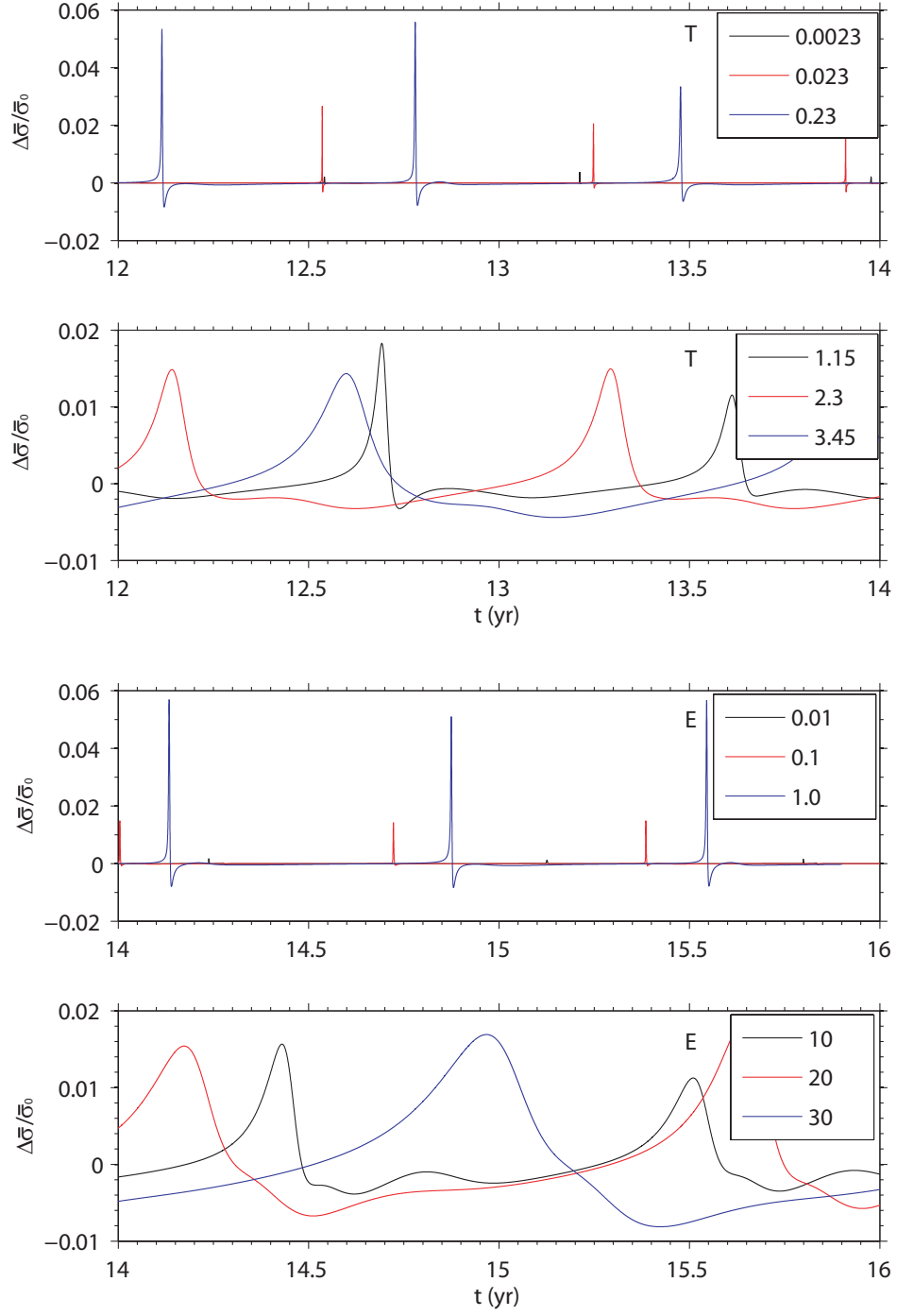


Figure 4: Effective normal stress change  $\Delta\bar{\sigma}$ , normalized by the initial  $\bar{\sigma}_0$ , at  $\xi = W/4$ , for simulated sequences of aseismic slip events. (a)  $E = 1$  fixed.  $T = 0.0023, 0.023$  and  $0.23$ . The amplitude and duration of pore suction and the following recovery increase as  $T$  becomes higher. (b)  $E = 1$  fixed.  $T = 1.15, 2.3$  and  $3.45$ . (c)  $T = 0.23$  fixed.  $E = 0.01, 0.1$  and  $1.0$ . (d)  $T = 0.23$  fixed.  $E = 10, 20$  and  $30$ .



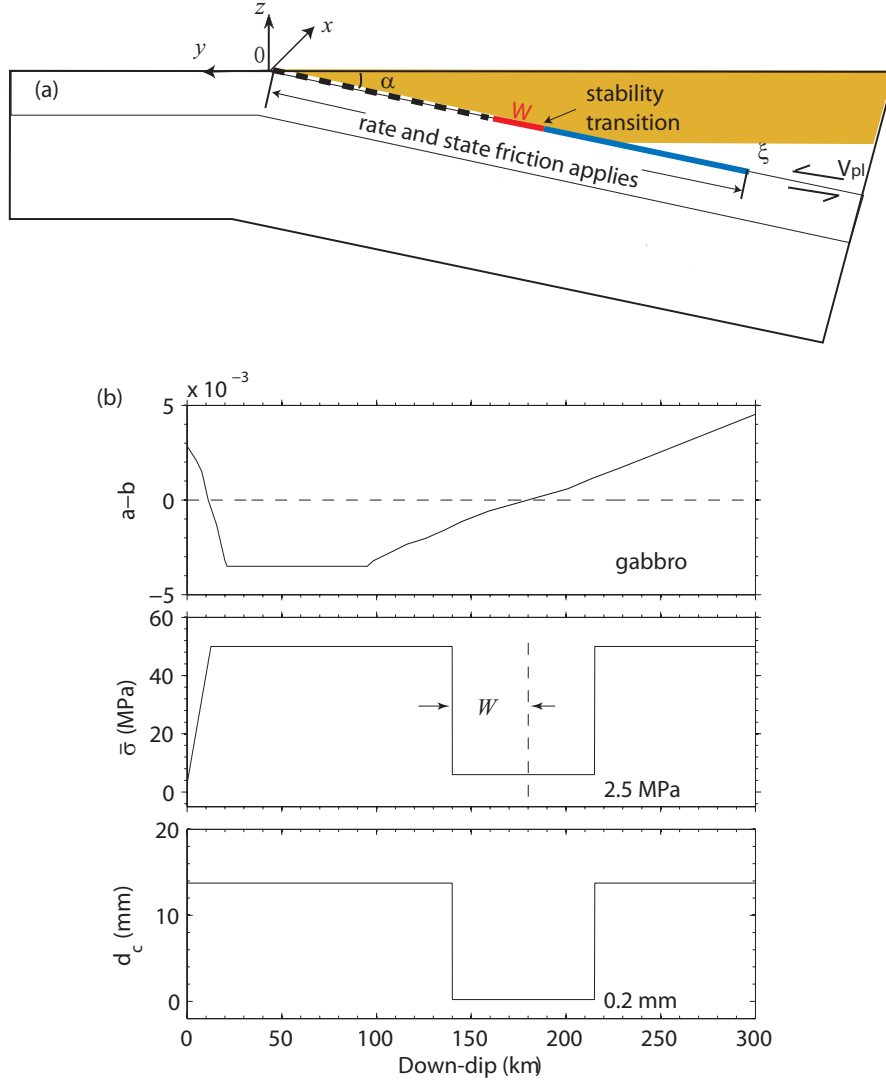


Figure 5: (a) Two-dimensional subduction fault model. The thrust fault is simulated by a planar frictional interface dipping at  $12^\circ$  in an elastic half-space.  $\xi$  is distance along down-dip direction. Rate and state friction applies from surface  $\xi = 0$  to  $\xi = W' = 300$  km, with depth-variable friction parameters. Fault is loaded by a constant plate rate  $V_{pl} = 37$  mm/yr down-dip from  $\xi = W'$ . Properties are uniform along the strike direction  $x$  (perpendicular to  $y - z$  plane). Bold red line represents the velocity-weakening fault of length  $W$  up-dip from the stability transition under low effective normal stress. Friction parameter  $a - b$ , effective normal stress  $\bar{\sigma}$  and characteristic evolution distance  $d_c$  down-dip distributions using the gabbro friction data are shown in (b). (b) Down-dip distributions of friction parameter  $a - b$ , initial effective normal stress  $\bar{\sigma}_0$  and characteristic evolution distance  $d_c$  for models using gabbro friction data. Temperature-dependent  $a - b$  from *He et al.* [2007] experiments are mapped to be depth-dependent using a Cascadia thermal model by *Peacock et al.* [2002]. Lower friction stability transition is at  $\sim 180$  km.  $W$  is the distance up-dip from stability transition with low  $\bar{\sigma}_0$ .

$\langle b - a \rangle$  is the average  $b - a$  over  $W$ . For the  $a - b$  distribution shown in Figure 5(b), model parameters  $W$ ,  $\bar{\sigma}_0$  and  $d_c$  in the low effective normal stress zone are related via equation (3). We first choose  $W$  that is in a reasonable agreement with the petrologically and seismically estimated extent of near-lithostatic  $p$  region. That is a few tens of kilometers up-dip from the stability transition. For each fixed  $W$ ,  $\langle b - a \rangle$  is thus determined.  $\bar{\sigma}_0$  and  $d_c$  are then varied accordingly to result in a range of  $W/h^*$  that allow quasi-periodic aseismic events. On the rest of the fault,  $d_c$  is uniformly

$$d_c = \frac{\pi(b - a)_{max}\bar{\sigma}_0 h_0^*}{2\mu'}, \quad (19)$$

where  $(b - a)_{max} = 0.0035$  is the maximum velocity-weakening value, and  $h_0^*$  is a fixed factor (16 in all calculations) times the computational grid size to assure computed results are free from grid discretization effect. In the example shown in Figure 5(b),  $W = 40$  km,  $d_c = 0.2$  mm in the  $\bar{\sigma}_0 = 2.5$  MPa zone such that  $W/h^* \sim 16$ .  $d_c = 13.74$  mm elsewhere on the fault.

#### 4.1 2-D results without dilatancy

A general fault response to the above loading conditions and model parameters is that megathrust earthquakes rupture the entire seismogenic zone every few hundred years, and quasi-periodic aseismic transients, mostly limited to within the low  $\bar{\sigma}_0$  zone, appear every a few years in the interseismic period.

Four groups of calculations with  $W = 35, 40, 50$  and  $55$  km are performed in the range of  $W/h^* = 6$  to  $16$ , which allows spontaneous aseismic transients. Three representative properties of transients: maximum slip velocity  $V_{max}$ , slip  $\delta$  at the center of  $W$  accumulated when  $V_{max}$  exceeds  $2V_{pl}$ , and recurrence period  $T_{cyc}$ , vary significantly for a wide spectrum of choices of  $W$ , low  $\bar{\sigma}_0$  and  $d_c$ . The general trend is that all three properties increase with  $W/h^*$ , which has also been observed from calculations using the wet granite friction data [Blanpied *et al.*, 1998], and is shown in Figure 7 (solid gray symbols) for reference. At the same  $W/h^*$ , variations with different choices of  $W$  are relatively large, compared to those using the granite data, because the velocity-weakening  $a - b$  follows a gradual increase to neutral stability over the entire length of  $W$ . Detailed discussions of modeled transient properties and comparison of calculated surface deformation to GPS observations in northern Cascadia can be found in Liu and Rice [2009].

#### 4.2 2-D results with dilatancy

The introduction of  $E$  and  $T$  adds to the vast parameter space that needs to be explored to model the properties of slow slip events. In this paper, we use a constant  $W = 40$  km, which, in combination with appropriate choices of  $\bar{\sigma}_0$  and  $d_c$ , has been shown to produce surface deformations in reasonable agreement with GPS observations in northern Cascadia [Liu and Rice, 2009]. Furthermore, with the knowledge that fault response approaches the non-dilatancy situation at  $T \ll 1$  and steady state at  $T \gg 1$  (Figure 3), we focus on the intermediate degree of drainage, that is,  $T$  of order unity.

Figure 6 shows sequences of slow slip events for 100 years within the interseismic period, using parameters  $W = 40$  km,  $\bar{\sigma}_0 = 2.5$  MPa and  $d_c = 0.2$  mm (thus  $W/h^* \sim 16$ ), as shown in Figure 5(b), and  $(\epsilon/\beta)/\bar{\sigma} = 0.04$  ( $\epsilon/\beta = 0.1$  MPa and  $E = 0.63$  in the low  $\bar{\sigma}_0$  zone). Two megathrust earthquakes occur at  $\sim 224$  yr and  $655$  yr, with the maximum seismic velocity about  $0.1$  m/s (not shown here). In the interseismic period,  $V_{max}$  oscillates between  $V_{pl}$  and the peak

aseismic rate of  $\sim 10V_{pl}$ , which is nearly 3 orders of magnitude smaller than its counterpart without dilatancy. The middle panel shows slip  $\delta$  at the center of  $W$  accumulated during each episode when  $V_{max}$  exceeds  $2V_{pl}$ . The bottom panel shows the recurrence period  $T_{cyc}$ , defined as the interval between two successive events when  $V_{max}$  reaches the peak values. The moderate variations in  $\delta$  and  $T_{cyc}$  are due to the interseismic strength evolution, including evolution of pore pressure, in the low  $\bar{\sigma}$  zone and up-dip in the nearly locked zone. From the selected interseismic time windows that are free of the earthquake nucleation and postseismic relaxation effects, we make the histograms of  $\delta$  and  $T_{cyc}$ , identify their maximum likelihood values and record the maximum and minimum of each property as its variation range.

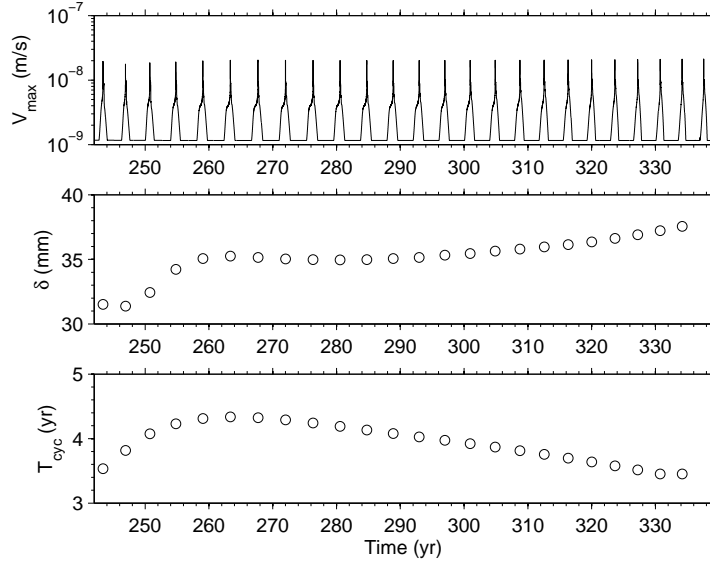


Figure 6: Spontaneous short-period slow slip events in a 100-yr interseismic period, using gabbro friction data. Initial  $\bar{\sigma}$  and  $d_c$  distributions are shown in Figure 5(b). In the low  $\bar{\sigma} = 2.5$  MPa zone, dilatancy parameter  $\epsilon/\beta = 0.1$  MPa (thus  $(\epsilon/\beta)/\bar{\sigma} = 0.04$ ), corresponding to open red diamond at  $W/h^* \sim 16$  in Figure 7), drainage  $T = t_p/(d_c/V_{ss}) = 0.23$ . (Top) Maximum slip rate. (Middle) Cumulative slip at the center of velocity-weakening low  $\bar{\sigma}_0$  zone, when  $V_{max} > 2V_{pl}$ . (Bottom) Recurrence interval.

Using constant  $W = 40$  km and  $T = 0.23$ , three groups of calculations with  $(\epsilon/\beta)/\bar{\sigma}_0 = 0.02, 0.04$  and  $0.1$  in the low  $\bar{\sigma}_0$  zone, corresponding to an average  $E = 0.31, 0.63$  and  $1.57$  respectively are summarized (open diamond symbols) in Figure 7. Outside the low  $\bar{\sigma}_0$  zone, a uniform  $\epsilon/\beta = 0.1, 0.2$  and  $0.5$  MPa is used, respectively, so that the influence from earthquakes is roughly the same. For reference, solid gray symbols represent results from calculations without dilatancy; spontaneous aseismic events are present within the range  $W/h^* \sim 6$  to  $16$  [Liu and Rice, 2009]. For each group of  $(\epsilon/\beta)/\bar{\sigma}_0$  (constant  $E$ ),  $\bar{\sigma}_0$  and  $d_c$  are varied according to equation (17) to result in  $W/h^* \approx 8, 12.8 \dots 48$ . The cumulative aseismic slip  $\delta$  and recurrence period  $T_{cyc}$  both increase with  $W/h^*$  (Figure 7(a) and (b)), following the trend of the non-dilatancy situation. The lower limit of  $W/h^*$  for the onset of spontaneous aseismic transients is slightly larger in the dilatancy situation due to its stabilizing effect. Dramatic differences exist in the maximum velocity reached during transients. For example, without dilatancy  $V_{max}$  quickly approaches seismic rate ( $> 10^{-3}$  m/s  $\sim 10^6 V_{pl}$ ) as  $W/h^*$  increases toward  $16$ , while  $V_{max}$  is less than  $10^2 V_{pl}$  at the same  $W/h^*$  with dilatancy. The stabilizing effect is more prominent as  $W/h^*$  increases beyond the no-

dilatancy boundary; at  $W/h^* \sim 32$ ,  $V_{max} \approx 10^{2.8}V_{pl}$  for  $(\epsilon/\beta)/\bar{\sigma}_0 = 0.02$  and  $V_{max} \approx 10^{1.3}V_{pl}$  for  $(\epsilon/\beta)/\bar{\sigma}_0 = 0.1$ . For the small  $(\epsilon/\beta)/\bar{\sigma}_0 = 0.02$ ,  $\log_{10}(V_{max}/V_{pl})$  approximately follows a linear increasing trend with  $W/h^*$ , which is supported by  $V_{max} \sim 5 \times 10^{-5} \text{ m/s} \sim 10^{4.5}V_{pl}$  at  $W/h^* \sim 64$  (not shown in Figure 7). Following such a linear trend, seismic rate can be reached at  $W/h^* \sim 80$ . The rate at which  $V_{max}$  increases with  $W/h^*$  becomes smaller for larger  $(\epsilon/\beta)/\bar{\sigma}_0$ . In particular, for calculations with the same  $(\epsilon/\beta)/\bar{\sigma}_0$  (e.g., 0.1), the  $\log_{10}(V_{max}/V_{pl})$  versus  $W/h^*$  trend appears to approach a plateau, indicating aseismic slip at infinitely large  $W/h^*$ .

Figure 8 illustrates the slip velocity and pore pressure evolution during one modeled transient event, with dilatancy parameters  $T = 1.0$ ,  $(\epsilon/\beta)/\bar{\sigma}_0 = 0.04$  in the low  $\bar{\sigma}_0 = 2.5 \text{ MPa}$  and  $d_c = 0.2 \text{ mm}$  zone. Only the depth range involved in the transient slip is plotted. The friction stability transition is at down-dip 180 km, and the low  $\bar{\sigma}_0$  zone extends from 140 to 215 km. A major nucleation front first appears at down-dip  $\sim 170 \text{ km}$  and migrates up-dip within the low  $\bar{\sigma}$  zone long before the maximum velocity is reached. A secondary nucleation front, with smaller velocity and slower down-dip migration speed, shows up when the major nucleation front has reached down-dip  $\sim 155 \text{ km}$ . After the two nucleation fronts merge and reach a maximum velocity of  $\sim 2.5 \times 10^{-8} \text{ m/s}$ , slip propagates in both up-dip and down-dip directions along the fault. The up-dip propagation continues for a short distance before it encounters the abrupt increase to  $\bar{\sigma}_0 = 50 \text{ MPa}$ ; meanwhile the down-dip propagation extends to the stability transition before the velocity decreases to be around  $V_{pl}$ . Both the propagation speed and sliding velocity are comparable along the up-dip and down-dip directions, suggesting approximate stress drops associated with the slow slips. The general feature of pore pressure variation, as represented by  $\Delta\bar{\sigma} = -(p - p_0)$  in Figure 8(b), is very similar to those of slip velocity evolution in (a) as the change in  $p$  is directly related to the change in state variable by equation (10). Along the major nucleation front, pore pressure drops as the fault slips faster due to the increased porosity and insufficient fluid supply in the corresponding state evolution time scale to refill the pores. As the nucleation front passes by and velocity returns to the level near  $V_{pl}$ , we observe a transient phase of pore pressure rise of a smaller amplitude because the magnitude of the velocity drop is smaller than that of the velocity rise associated with the nucleation front. Along the down-dip propagation front, pore pressure drop and rise are of the similar amplitude ( $< \sim 0.05 \text{ MPa}$ ), as a result of similar magnitude of velocity increase and subsequent decrease.

## 5. Conclusions

Frictional and hydraulic conditions for spontaneous aseismic deformation transients are analyzed on a fluid-infiltrated fault including dilatancy and pore compaction in the framework of rate- and state-dependent friction, with the “membrane diffusion” approximation.

Using a simplified model fault which is locked at one end and loaded with a constant rate at the other end (the locked and loaded segments are much longer than the part where rate and state friction applies), we found that with dilatancy aseismic transients can exist beyond the aseismic-seismic boundary that is defined in the absence of dilatancy. The ratio between the length of the fault that slides at velocity-weakening under high fluid pressure and the critical nucleation patch size  $W/h^*$  continues to be an important parameter. Simple periodic, period doubling, aperiodic aseismic oscillations appear as  $W/h^*$  increases. Both the transients maximum slip velocity and the recurrence period increase with  $W/h^*$ , with the more significant variations at larger  $W/h^*$ . Two other important parameters are (1)  $T = t_p/(d_c/V_{ss})$ , the ratio between the characteristic diffusion

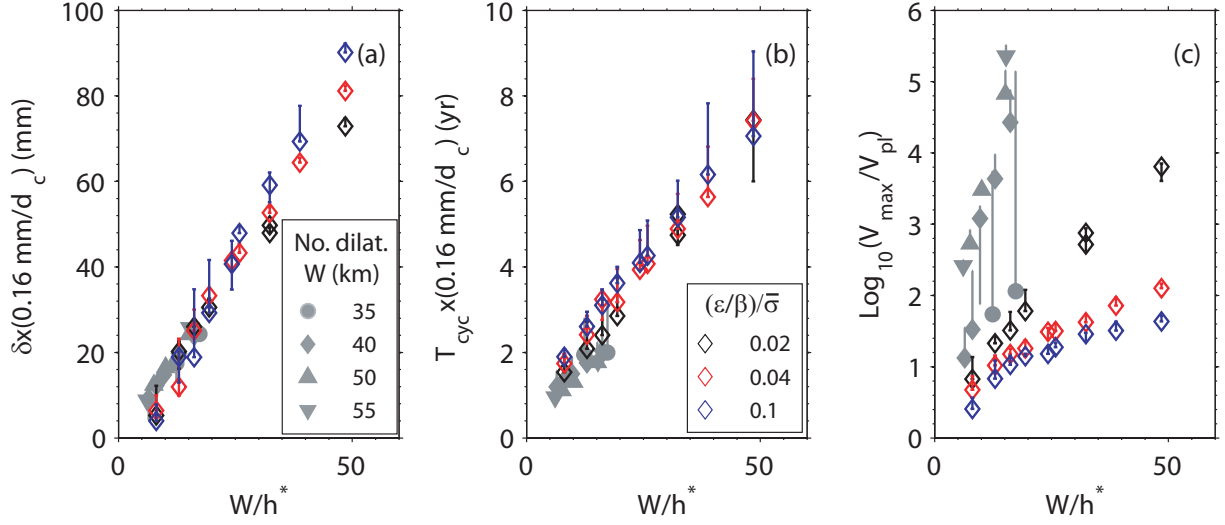


Figure 7: Exploration in the parameter space, using gabbro friction data, shows that cumulative slip, recurrence interval and maximum velocity of modeled SSEs all increase with  $W/h^*$ . Solid gray symbols represent simulation cases using  $W = 35, 40, 50$  and  $55$  km, respectively, without dilatancy effect for reference. Open diamond symbols are cases using a fixed  $W = 40$  km, drainage  $T = 0.23$  and different dilatancy parameters  $(\epsilon/\beta)/\bar{\sigma} = 0.02$  (black),  $0.04$  (red) and  $0.1$  (blue), corresponding to an average  $E = 0.31, 0.63$  and  $1.57$ , respectively, in the low  $\bar{\sigma}$  zone. Variations in  $\delta$ ,  $T_{cyc}$  and  $V_{max}$  for each case, as shown in Figure 6, are represented by error bars.  $\delta$  and  $T_{cyc}$  are labeled such that they can also be interpreted for other choices of  $d_c$ .

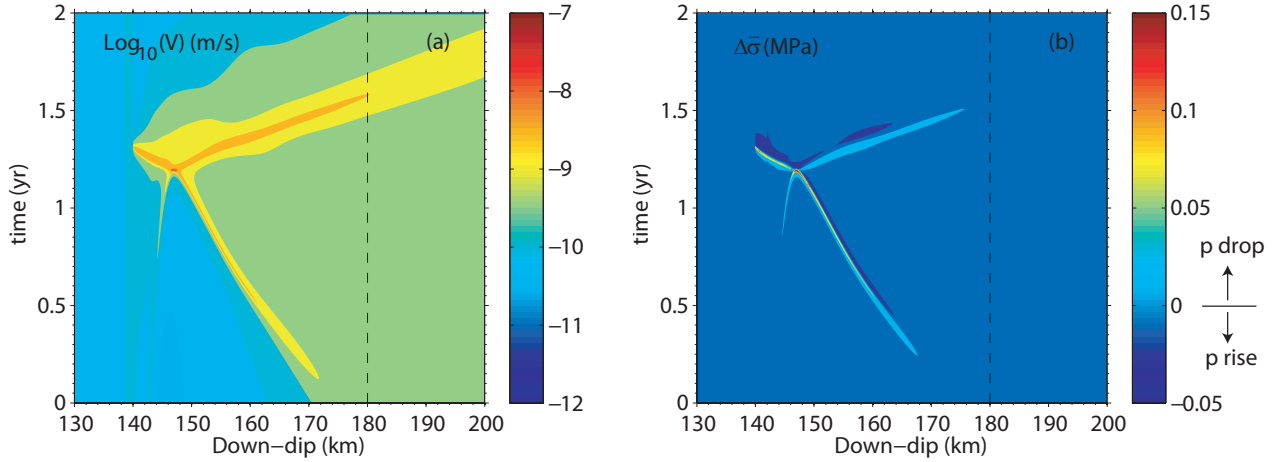


Figure 8: (a) Slip velocity and (b) pore pressure, represented by  $\Delta\bar{\sigma} = -(p - p_0)$ , during a modeled transient event, using  $W = 40$  km, low  $\bar{\sigma} = 2.5$  MPa and  $d_c = 0.2$  mm ( $W/h^* \sim 16$ ). Dilatancy related parameters are  $T = 0.23$ ,  $(\epsilon/\beta)/\bar{\sigma} = 0.04$  ( $E = 0.63$ ) in the low  $\bar{\sigma}$  zone, and  $\epsilon/\beta = 0.2$  MPa at depths with high  $\bar{\sigma} = 50$  MPa. Vertical dashed line points the position of velocity-weakening to strengthening stability transition.

time scale for pore pressure  $p$  on the sliding interface to equilibrate with its ambient level and the state variable evolution time scale at steady state velocity, and (2)  $E = f_0(\epsilon/\beta)/(b\bar{\sigma}_0)$  which measures the relative contributions to the peak-to-residual stress drop from pore suction and from friction evolution. We showed that parameters  $T$  and  $E$  have similar effects on the maximum velocity  $V_{max}$  and recurrence period  $T_{cyc}$  of modeled aseismic transients.  $V_{max}$  decreases as  $T$  or  $E$  increases toward 1.  $T_{cyc}$  remains relatively constant for  $T$  (or  $E$ ) less than 1, due to the compensation effects of smaller velocity and longer sliding duration.  $T_{cyc}$  increases for  $T$  (or  $E$ ) greater than 1, as the pore suction amplitude remains nearly constant but for a longer duration. The variation of  $T_{cyc}$  with  $T$  and  $E$  can be explained the analytical neutral stability period  $T_{ns}$  that is derived for a single-degree-of-freedom spring-slider system with dilatancy.

Using a Cascadia-like 2-D subduction fault model with the rate and state frictional properties measured for gabbro gouges under hydrothermal conditions, we showed that episodic aseismic transients can also exist for a much broader range of  $W/h^*$  due to dilatancy stabilization. The cumulative slip per episode  $\delta$  and the recurrence period  $T_{cyc}$  of modeled transients are comparable to those at the same  $W/h^*$  without dilatancy. They further follow the approximately linear trend of increasing  $\delta$  and  $T_{cyc}$  beyond the aseismic-seismic boundary defined under the no-dilatancy condition. In contrast,  $V_{max}$  during transients can be several orders of magnitude smaller than those at the same  $W/h^*$  without dilatancy. The difference in  $V_{max}$  becomes more significant at large  $W/h^*$ .

## Publications resulting from work carried out under this award

Liu, Y., A. M. Rubin, and J. R. Rice, Role of fault gouge dilatancy in subduction zone aseismic deformation transients, submitted to *J. Geophys. Res.*, accepted pending minor revisions 05/07/2010.

Segall, P., A. M. Rubin, A. M. Bradley, and J. R. Rice, Dilatant strengthening as a mechanism for slow slip events, submitted to *J. Geophys. Res.*, accepted pending minor revisions.

## References

- Ampuero, J.-P., and A. M. Rubin (2008), Earthquake nucleation on rate and state faults c aging and slip laws, *J. Geophys. Res.*, 113(B01302), doi:10.1029/2007JB005082.
- Audet, P., M. G. Bostock, N. I. Christensen, and S. M. Peacock (2009), Seismic evidence for overpressured subducted oceanic crust and megathrust fault sealing, *Nature*, 457, 76–78, doi: 10.1038/nature07650.
- Blanpied, M. L., C. J. Marone, D. A. Lockner, J. D. Byerlee, and D. P. King (1998), Quantitative measure of the variation in fault rheology due to fluid-rock interactions, *J. Geophys. Res.*, 103(B5), 9691–9712.
- Clarke, G. K. C. (1987), Subglacial till: A physical framework for its properties and processes, *J. Geophys. Res.*, 92, 9023–9036.
- Dragert, H., K. Wang, and T. S. James (2001), A silent slip event on the deeper cascadia subduction interface, *Science*, 292(5521), 1525–1528.



- He, C., Z. Wang, and W. Yao (2007), Frictional sliding of gabbro gouge under hydrothermal conditions, *Tectonophysics*, *445*, 353–362, doi:10.1016/j.tecto.2007.09.008.
- Hirose, H., K. Hirahara, F. Kimata, N. Fujii, and S. Miyazaki (1999), A slow thrust slip event following the two 1996 Hyuganada earthquakes beneath the Bungo Channel, southwest Japan, *Geophys. Res. Lett.*, *26*(21), 3237–3240.
- Iverson, N. R., T. S. Hooyer, and R. W. Baker (1998), Ring-shear studies of till deformation: Coulomb-plastic behavior and distributed strain in glacier beds, *J. of Glaciology*, *44*, 634–642.
- Iverson, R. M., M. E. Reid, N. R. Iverson, R. G. LaHusen, M. Logan, J. E. Mann, and D. L. Brien (2000), Acute sensitivity of landslide rates to initial soil porosity, *Science*, *290*, 513–516.
- Lachenbruch, A. H. (1980), Frictional heating, fluid pressure, and the resistance to fault motion, *J. Geophys. Res.*, *85*, 6097–6112.
- Lapusta, N., J. R. Rice, Y. Ben-Zion, and G. Zheng (2000), Elastodynamic analysis for slow tectonic loading with spontaneous rupture episodes on faults with rate- and state-dependent friction, *J. Geophys. Res.*, *105*(B10), 23,765–23,789.
- Liu, Y., and J. R. Rice (2005), Aseismic slip transients emerge spontaneously in three-dimensional rate and state modeling of subduction earthquake sequences, *J. Geophys. Res.*, *110*(B08307), doi:10.1029/2004JB003424.
- Liu, Y., and J. R. Rice (2005b), Pore pressure evolution in shallow subduction earthquake sequences and effects on aseismic slip transients - Numerical modeling with rate and state friction, *Eos Trans. AGU*, *86*(52), Fall Meet. Suppl., Abstract T11E–05.
- Liu, Y., and J. R. Rice (2007), Spontaneous and triggered aseismic deformation transients in a subduction fault model, *J. Geophys. Res.*, *112*(B09404), doi:10.1029/2007JB004930.
- Liu, Y., and J. R. Rice (2009), Slow slip predictions based on granite and gabbro friction data compared to GPS measurements in northern Cascadia, *J. Geophys. Res.*, *in press*.
- Lockner, D. A., and J. D. Byerlee (1994), Dilatancy in hydraulically isolated faults and the suppression of instability, *Geophys. Res. Lett.*, *21*, 2353–2356.
- Lowry, A. R., K. M. Larson, V. Kostoglodov, and R. Bilham (2001), Transient fault slip in Guerrero, southern Mexico, *Geophys. Res. Lett.*, *28*(19), 3753–3756.
- Marone, C., C. B. Raleigh, and C. H. Scholz (1990), Frictional behavior and constitutive modeling of simulated fault gouge, *J. Geophys. Res.*, *95*(B5), 7007–7025.
- Mase, C. W., and L. Smith (1987), Effects of frictional heating on the thermal, hydrologic, and mechanical response of a fault, *J. Geophys. Res.*, *92*, 6249–6272.
- Peacock, S. M., K. Wang, and A. M. McMahon (2002), Thermal structure and metamorphism of subducting oceanic crust: Insight into cascadia intraslab earthquakes, in *The Cascadia subduction zone and related subduction systems: Seismic structure, Intraslab earthquakes and processes, and earthquake hazards*, edited by S. Kirby, K. Wang, and S. Dunlop, pp. 123–126, U. S. Geol. Surv. Open-File Rep., 02-328 and Geol. Surv. Canada Open-File, 4350.

- Rice, J. R. (1993), Spatiotemporal complexity of slip on a fault, *J. Geophys. Res.*, 98(B6), 9885–9907.
- Rice, J. R., N. Lapusta, and K. Ranjith (2001), Rate and state dependent friction and the stability of sliding between elastically deformable solids, *J. Mech. Phys. Solids*, 49, 1865–1898.
- Rubin, A. M. (2008), Episodic slow slip events and rate-and-state friction, *J. Geophys. Res.*, (B11414), doi:10.1029/2008JB005642.
- Rubin, A. M., and J.-P. Ampuero (2005), Earthquake nucleation on (again) rate and state faults, *J. Geophys. Res.*, (B11312), doi:10.1029/2005JB003686.
- Rudnicki, J. W., and C.-H. Chen (1988), Stabilization of rapid frictional slip on a weakening fault by dilatant hardening, *J. Geophys. Res.*, 93, 4745–4757.
- Samuelson, J., D. Elsworth, and C. Marone (2008), Modeling the effect of quasi-drained fault zone dilatancy on friction constitutive properties, *Eos Trans. AGU*, 89(52), Fall Meet. Suppl., Abstract S41A–1821.
- Schofield, A. N., and C. P. Wroth (1968), *Critical state soil mechanics*, McGraw-Hill, New York.
- Segall, P., and J. R. Rice (1995), Dilatancy, compaction, and slip instability of a fluid-infiltrated fault, *J. Geophys. Res.*, 100(B11), 22,155–22,171.
- Segall, P., and A. Rubin (2007), Dilatancy stabilization of frictional sliding as a mechanism for slow slip events, *Eos Trans. AGU*, 88(52), Fall Meet. Suppl., Abstract T13F–08.
- Segall, P., A. M. Rubin, A. M. Bradley, and J. R. Rice (2010), Dilatant strengthening as a mechanism for slow slip events, *J. Geophys. Res.*, submitted.
- Shibazaki, B., and T. Shimamoto (2007), Modelling of short-interval silent slip events in deeper subduction interfaces considering the frictional properties at the unstable-stable transition regime, *Geophysical Journal International*, 171(1), 191–205, doi:10.1111/j.1365-246X.2007.03434.x.
- Sibson, R. H. (1973), Interactions between temperature and pore fluid pressure during earthquake faulting and a mechanism for partial or total stress relief, *Nature*, 243(126), 66 – 68.
- Sleep, N. H. (1995), Ductile creep, compaction, and rate and state dependent friction within major fault zones, *J. Geophys. Res.*, 100, 13,065–13,080.
- Sleep, N. H., and M. L. Blanpied (1992), Creep, compaction and the weak rheology of major faults, *Nature*, 359(6397), 687–692.
- Taylor, M. A. J., and J. R. Rice (1998), Dilatant stabilization of subduction earthquake rupture into shallow thrust interface, *Eos Trans. AGU*, 79(45), Fall Meet. Suppl., p. F631.